Opto-Electronic Advances

CN 51-1781/TN ISSN 2096-4579 (Print) ISSN 2097-3993 (Online)

Non-volatile tunable multispectral compatible infrared camouflage based on the infrared radiation characteristics of Rosaceae plants

Xin Li, Xinye Liao, Junxiang Zeng, Zao Yi, Xin He, Jiagui Wu, Huan Chen, Zhaojian Zhang, Yang Yu, Zhengfu Zhang, Sha Huang and Junbo Yang

Citation: Li X, Liao XY, Zeng JX, et al. Non-volatile tunable multispectral compatible infrared camouflage based on the infrared radiation characteristics of Rosaceae plants. *Opto-Electron Adv* **8**, 250031(2025).

https://doi.org/10.29026/oea.2025.250031

Received: 25 February 2025; Accepted: 16 May 2025; Published online: 9 July 2025

Opto-Electronic Advances

Article

August 2025, Vol. 8, No. 8

DOI: 10.29026/oea.2025.250031 CSTR: 32247.14.oea.2025.250031

Non-volatile tunable multispectral compatible infrared camouflage based on the infrared radiation characteristics of Rosaceae plants

Xin Li[1†], Xinye Liao[1†], Junxiang Zeng[1†], Zao Yi[2], Xin He[1*], Jiagui Wu[3*], Huan Chen[1], Zhaojian Zhang[1], Yang Yu[1], Zhengfu Zhang[1], Sha Huang[1] and Junbo Yang[1*]

Most multispectral compatible infrared camouflage devices primarily focus on achieving low emissivity but neglect environmental emissivity matching when environmental emissivity exceeds that of the devices, this creates a "low-emissivity exposure" risk. To address this issue, we develop a tunable multispectral compatible infrared camouflage device using phase change material In_3SbTe_2 (IST). Simulation and experimental results demonstrate that in both the amorphous (aIST) and crystalline (cIST) states, the device achieves simulated plant infrared camouflage and ultra-low emissivity infrared camouflage within the atmospheric window bands (3–5 μm and 8–14 μm). To address thermal management, it utilizes two non-atmospheric window bands (2.5–3 μm and 5–8 μm) for heat dissipation. Additionally, laser stealth is realized at three specific wavelengths (1.064 μm, 1.55 μm, and 10.6 μm). In the visible spectrum, high absorptivity enables effective visible light camouflage. Adjusting the geometric parameters of top layer structure enables color variation. This work not only highlights potential applications in reversible switching, reconfigurable imaging, and dynamic coding using IST but also offers an effective strategy to counter multispectral detection technology.

Keywords: multispectral compatible infrared camouflage; phase change; laser stealth; heat management; color variation

Li X, Liao XY, Zeng JX et al. Non-volatile tunable multispectral compatible infrared camouflage based on the infrared radiation characteristics of Rosaceae plants. *Opto-Electron Adv* **8**, 250031 (2025).

Introduction

Advancements in micro- and nano-optics research have enabled precise control over various optical bands through the use of metamaterials[1–5], paving the way for diverse functional applications across visible, infrared, terahertz, and microwave spectra. Infrared camouflage technology aims to reduce the detectability of the target in the infrared spectrum as an important component of stealth technology, thereby enhancing their survivability. However, the evolution of infrared detection technology, particularly the integration of multispectral detection methods, has introduced new challenges to target concealment. To address these challenges, research into multispectral compatible infrared camouflage

[1]College of Science, National University of Defense Technology, Changsha 410073, China; [2]Joint Laboratory for Extreme Conditions Matter Properties, Southwest University of Science and Technology, Mianyang 621010, China; [3]School of Physical Science and Technology, Southwest University, Chongqing 400715, China.

[†]These authors contributed equally to this work.

*Correspondence: X He, E-mail: hexin12a@nudt.edu.cn; JG Wu, E-mail: mgh@swu.edu.cn; JB Yang, E-mail: yangjunbo@nudt.edu.cn

Received: 25 February 2025; Accepted: 16 May 2025; Published online: 9 July 2025

technology[6–13] has become increasingly vital. According to Stefan-Boltzmann's law[14,15], the intensity of thermal radiation is primarily influenced by two factors: surface emissivity and surface temperature. Consequently, thermal infrared camouflage can be achieved by strategically controlling these parameters. Typically, the thermal radiation of a target exceeds that of its background, necessitating the suppression of the target's thermal radiation signal within the two primary thermal infrared detection bands, corresponding to the atmospheric windows of 3–5 μm and 8–14 μm.

The prevailing research on multispectral compatible infrared camouflage predominantly encompasses visible light, near-infrared, and microwave spectra. In the realm of visible light camouflage[16–19], the primary objective is to either achieve high absorptivity or high transparency in the visible light band, or to seamlessly blend with the color of the surrounding environment. For near-infrared camouflage[20–23], the emphasis is on diminishing the reflection of natural light sources, such as sunlight and moonlight, as well as artificial light sources such as laser. The research on microwave camouflage[24–29], the primary focus is on attenuating the echo signal through mechanisms of absorptivity or scattering. Therefore, multispectral compatible camouflage technology requires the target to achieve camouflage effects across two or more wave bands. Zhang et al.[30] and Liu et al.[31] used one-dimensional Ge/ZnSe photonic crystal to attain low emissivity in the 3–5 μm and in the 8–14 μm, while also achieving thermal management in the 5–8 μm. Furthermore, they utilized the top ZnSe layer and the MgF_2/ZnSe/MgF_2/ZnSe layer for color variation. Liu et al.[31] reduced the reflectivity in the near-infrared band by incorporating the MgF_2/ZnSe/MgF_2/ZnSe layer on the top of a Ge/ZnSe photonic crystal, resulting in the reflectivity of less than 0.03 for 1.06 μm laser wavelength. Deng et al.[32] achieved the low emissivity in the thermal infrared band using the Ge/ZnS photonic crystal. The addition of the YbF_3/ZnS/Ge/ZnS film at the top resulted in the reduced reflectivity in the visible band to 2.67%. The average reflectivity of the photonic crystal structure is only 9% in the range of 300–1100 nm. Park et al.[20] utilized a metal-dielectric-metal structure to achieve low emissivity in the 3–5 μm and 8–14 μm, while also implementing thermal management in the 5–8 μm. Broadband absorptivity in the near-infrared band was realized through the resonance effect of the top metal structure. Kim et al.[33] combined an infrared selective radiator with a microwave frequency selective absorber. The authors not only achieved low emissivity in the 3–5 μm and 8–14 μm, and thermal management in the 5–8 μm, but also realized high absorptivity (>90%) in the 8–12 GHz band. Furthermore, by optimizing the microwave absorber structure, the microwave absorptivity band can be extended to 2–12 GHz[34]. But the current multispectral compatible infrared camouflage is mainly focused on how to achieve low infrared emissivity[20,30–32]. From the aspect of environmental factors, if the environmental emissivity is higher than that of the target, then the target is at risk of "low-emissivity exposure". Therefore, designing device that match the environment is crucial.

Traditional infrared camouflage materials frequently depend on specialized coatings or structural designs to modify their optical properties. However, the incorporation of phase change materials significantly expands the scope of infrared camouflage application. Phase change materials can alter their lattice structures in response to external stimuli, thereby bringing about significant differences in electrical and optical properties between different phase states. The continuous and reversible regulation of phase change materials between different lattice structures can be accomplished through methods such as gate voltage, heating, and optical energy injection[35–37]. For instance, Pan et al.[38] successfully achieved thermal infrared-visible compatible camouflage utilizing the metal micro-nanostructure. They deposited a GST thin film on the gold film, which resulted in low emissivity in the 3–5 μm and 8–14 μm , and high emissivity in the 5–8 μm. Furthermore, they demonstrated the ability to manipulate GST to achieve 10.6 μm laser stealth. The visible color change was achieved by regulating the top Si thin film. Zhou et al.[39] utilized phase change material IST to achieve the average emissivity variation of 94% in the mid-wave infrared (3–5 μm). By controlling the switch between the crystalline and amorphous states of IST, they realized infrared camouflage under different backgrounds. Liang et al.[40] used the phase change material VO_2 to regulate mid-wave and long-wave infrared. By controlling the switch between the metallic and dielectric states of VO_2, they were able to regulate the emissivity in the infrared band (5–13 μm) from 0.1 to 0.78. Zhou et al.[41] used phase change material IST to attain low emissivity in the 3–5 μm and 8–14 μm. By controlling the switching between the crystalline and amorphous states of the IST, they achieved dynamic tuning ranges of 0.8 and 0.9 in the 3–5 μm and 8–14 μm, respectively. The

color variation was achieved by preparing different thicknesses of films on the top layer. Research indicated that chalcogenide phase change materials (IST and GST) have faster switching speed and more stable property than VO_2 phase change material[42–45]. Compared IST with GST, IST exhibits better metallic property in the infrared spectrum, with the switching cycle of just 510 ns and the lifespan of over 10^8 [43]. However, current research on IST phase change, reversibility, and patterning is not sufficient. Achieving phase change, reversibility, and patterning of IST is still the current research focus.

To resolve the challenge of environmental emissivity matching and functional inflexibility in multispectral compatible infrared camouflage, this study employs Rosaceae plant radiation characteristics as the environmental emissivity reference and leverages phase change material IST to achieve tunable functionality. The design of the Cr/IST/Ge/TiO_2/Ge/ZnS (top layer cylinder) multispectral compatible infrared camouflage device is achieved using the finite difference time domain method and particle swarm optimization (PSO) algorithm. The Cr/IST film is prepared, and the laser experimental platform is set up to examine the phase change, reversibility, and patterning of phase change material IST. Simulation results indicate that the top ZnS layer only influences the near-infrared band, leaving the mid-wave infrared (3–5 μm) and long-wave infrared (8–14 μm) performance unaffected. Therefore, we use magnetron sputtering and electron beam evaporation processes to complete the device (no ZnS) and test the infrared spectrum and infrared camouflage (3–5 μm and 8–14 μm) performance. Both simulation and experiment results show excellent agreement. The cylindrical structure is then prepared through ion beam etching process, and the laser (1.064 μm, 1.55 μm, and 10.6 μm) stealth performance is tested and studied. Finally, color variations are achieved by modifying the geometric parameters of the top ZnS layer, without affecting the infrared performance of the device.

The design criterion of device

Rosaceae plant species hold significant importance due to their multifaceted values, including edible, ornamental, medicinal, and ecological functions. Their widespread cultivation across diverse regions is attributed to their strong ecological adaptability and high ornamental value. In this study, we investigate the infrared radiation characteristics of Rosaceae plants[46], providing the reference for device design. Figure 1(a) presents the infrared characteristics of various Rosaceae plants, revealing consistent radiation trends across species. Specifically, these plants exhibit relatively low absorptivity in the 3–5 μm and 8–14 μm bands, with higher absorptivity observed in the 3–5 μm range compared to the 8–14 μm band. Conversely, significantly higher absorptivity are evident in the 2.5–3 μm and 5–8 μm bands.

PSO algorithm design

Traditional approaches to device design frequently struggle to satisfy multi-objective optimization requirement. To address this limitation, we implement the particle swarm optimization (PSO) algorithm for device parameter optimization. While maintaining consistent material composition for each layer, we optimize three key parameters: the thickness (h) of individual membrane layer, and both the radius (R) and thickness (H) of the top cylindrical layer. For our optimization target, we focus on the crystalline state of IST as the primary objective, with the objective function defined as follows:

$$FOM=0.2\cdot R_1+0.3\cdot(1-R_2)+0.2\cdot R_3+0.1\cdot(1-R_4)+0.2\cdot((1-R_5)+(1-R_6))/2$$

1) The reflectivity characteristics are defined across multiple wavelength ranges: R_1 represents the average reflectivity in the 3–5 μm band, while R_2 corresponds to the average reflectivity in the 5–8 μm band. Similarly, R_3 denotes the average reflectivity across the 8–14 μm band, and R_4 characterizes the average reflectivity within the 2.5–3 μm band. For specific laser wavelengths, R_5 and R_6 represent the reflectivity values at 1.064 μm and 1.55 μm, respectively. The comprehensive optimization procedure is graphically presented in Fig. 2.

2) The device is designed with a bottom-to-top configuration of Cr/IST/Ge/TiO_2/Ge/ZnS. All material parameters are selected from established material libraries[47–49]. The optimization parameters include the thickness (h) of each individual layer, along with the radius (R) and thickness (H) of the top cylindrical layer. The thicknesses of each material layer (h and H) are limited to a maximum of 800 nm, because exceeding this thickness tends to induce issues resulting in film cracking. On the contrary, if the film is too thin to form a film, and the property is not stable. So we set the minimum membrane thickness as 50 nm. The radius (R) must not exceed 500 nm, while the structural period is fixed at 1 μm, since a smaller period will increase the fabrication difficulty.

3) Considering the performance of 10.6 μm wavelength in aIST state, compare the results from multiple

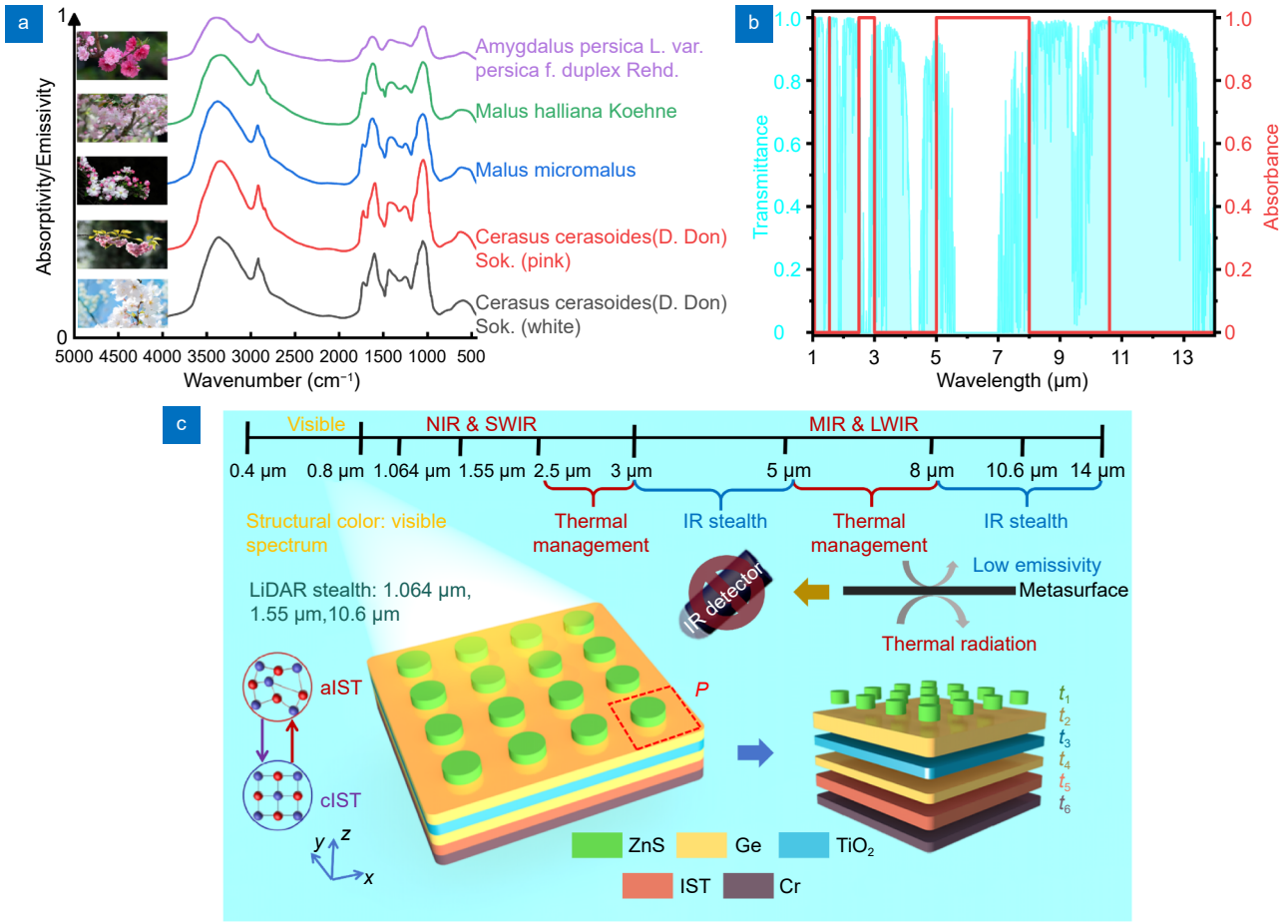

Fig. 1 | (**a**) The infrared emissivity curve of Rosaceae plants. (**b**) Atmospheric window transmission spectrum and ideal device spectrum. (**c**) Schematic diagram of the multispectral compatible infrared camouflage device.

outputs and select the optimal output as the best parameter.

During the optimization process, we employ the PSO algorithm combined with FDTD simulation for iterative optimization. To achieve multispectral compatible infrared camouflage, FOM function is established. According to Kirchhoff's law of thermal equilibrium, an object's emissivity equals to its absorptivity. As the substrate is metallic with zero transmittance, the sum of the object's absorptivity and reflectivity equals 1. Consequently, low emissivity (high reflectivity) is required in the 3–5 μm and 8–14 μm bands for infrared camouflage, while high emissivity (low reflectivity) is needed in the 2.5–3 μm and 5–8 μm bands to enable heat dissipation. High absorptivity is also essential for laser stealth at wavelengths of 1.064 μm, 1.55 μm, and 10.6 μm. Visible camouflage and color variation are achieved by adjusting the geometric parameters of the top structure.

First, the material types for each layer and the top layer model are fixed. The device from bottom to top is arranged as: Cr/IST/Ge/TiO_2/Ge/ZnS (top cylinder). The top ZnS layer primarily achieves visible camouflage, color variation, and near-infrared laser stealth (1.064 μm and 1.55 μm). The Ge/TiO_2/Ge forms an Metal-Insulator-Metal (MIM) structure to regulate infrared property in the 3–14 μm band, enabling low emissivity in the 3–5 μm and 8–14 μm bands and high emissivity in the 5–8 μm band. For the 2.5–3 μm band, the total film thickness matches the wavelength, with the underlying metal acting as a reflector to enhance absorptivity by multiple reflections. In the amorphous state of IST, the IST exhibits dielectric property, forming Fabry-Pérot resonance to enhance absorptivity at the 10.6 μm.

The algorithm optimizes the thickness of each layer as well as the radius and thickness of the top cylinder structure. Each optimization iteration calculates the FOM value. If the current FOM value exceeds the previous one, it replaces the prior FOM value and the updated FOM is output. If the current FOM value is lower, the algorithm triggers a reselection process. A cycle of 100 iterations outputs the current optimal FOM value. With the total

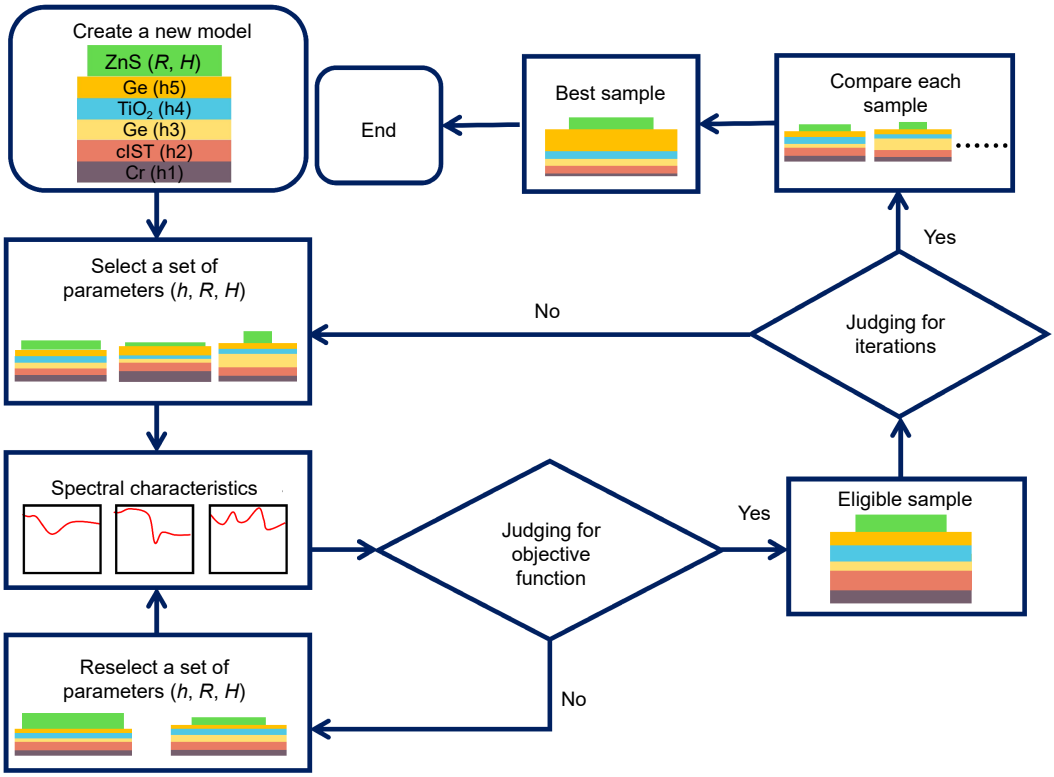

Fig. 2 | Design process of PSO algorithm.

number of iterations set to 100, the optimal FOM value is ultimately outputted as shown in Table 1.

Device design

We use the finite difference time domain method to simulate and design the device. The *x* and *y* directions are set as periodic layers, *z* direction is set as perfect match layer, with the mesh accuracy of 5 nm. The light source is incident on the surface of the device from the *z* direction. According to Kirchhoff's law of thermal equilibrium: under thermal equilibrium conditions, an object's emissivity is equivalent to its absorptivity. All simulation material parameters are all from the previous researches[47–49].

Device preparation

The sample fabrication process integrates three advanced techniques: magnetron sputtering, electron beam evaporation, and ion beam etching. For the electron beam evaporation process, we sequentially deposit Cr, Ge, TiO_2, and ZnS layers under precisely controlled conditions. The deposition is performed at a base pressure of 2×10^{-3} Pa, with respective evaporation rates of 0.5 nm/s for Cr, 0.5 nm/s for Ge, 0.2 nm/s for TiO_2, and 0.3 nm/s for ZnS, ensuring uniform film growth and precise thickness control. The IST process is conducted using magnetron sputtering under optimized parameters: the chamber pressure of 4×10^{-4} Pa, argon flow rate of 40 sccm, and the deposition rate maintained at 0.5 nm/s. During the fabrication process, no substrate baking is performed, and the substrate temperature remains equal to the chamber temperature. The chamber temperatures after depositing Cr, IST, Ge, TiO_2, and ZnS are 30 °C, 30 °C, 40 °C, 80 °C, and 28 °C, respectively. For the fabrication of the top ZnS nanostructure, we employ ion beam etching with precise energy control. The etching process is carried out at the acceleration voltage of 30 kV and an operating current of 80 pA.

Device characterization

Scanning Electron Microscopy (SEM) is employed to

Table 1 | Multispectral compatible infrared camouflage device parameters.

Layer	1	2	3	4	5	6	
Material	Cr	IST	Ge	TiO_2	Ge	ZnS	
Thickness (nm)	200	456	403	438	735	*R*=435	*H*=571

characterize the surface morphology and structural features. For infrared camouflage evaluation, we utilize an infrared detector (Guide Infrared G615Z) to assess performance in the 3–5 μm band, while an infrared thermal camera (Guide Infrared PS600) is used for measurements in the 8–14 μm band. Infrared spectroscopy measurement is conducted using the Nicolet Continuum Fourier Transform Infrared (FTIR) micro-area spectrometer, which provides precise spectral analysis. All optical components for the laser experiment platform are sourced from Lbtek (mirror: LPM05-532P-HP, diaphragm: DPP25, filter: CNDFR-50C-6M, beam splitter: MBS1455-A, prism: RAP125-A, convex lens: MCX20312-A, object lens: OPLN20X).

Results and discussion

The optimal parameters obtained from the PSO algorithm are used to plot the reflectivity spectra in Fig. 3(a). In the aIST state, the average emissivities in the 3–5 μm and 8–14 μm are both 0.28. For laser wavelengths of 1.064 μm, 1.55 μm and 10.6 μm, the absorptivity are 0.98, 0.92, and 0.94, respectively. In the cIST state, the average emissivities in the 3–5 μm and 8–14 μm are 0.25 and 0.14, respectively. For laser wavelengths of 1.064 μm and 1.55 μm, the corresponding absorptivity are 0.99 and 0.97, respectively. The average absorptivity for the 2.5–3 μm and 5–8 μm bands are 0.6 and 0.64, respectively. Furthermore, we compare the radiation intensity of the device in the two states at room temperature with that of blackbody radiation[50,51] (see Supplementary information of Fig. S1).

From the device design , the top ZnS layer mainly regulates the near-infrared (NIR 1–3 μm), while the following MIM structure controls both the mid-wave infrared (MIR 3–8 μm) and long-wave infrared (LWIR 8–14 μm). Figure 3(b) and 3(c) reveal that the top ZnS layer has a significant effect on the absorptivity/reflectivity at laser wavelengths of 1.064 μm and 1.55 μm. However, the influence on the average reflectivity in the 3–5 μm and 5–8 μm bands is minimal, with deviations around 4%, which has no significant effect on the infrared camouflage performance. Thus, the presence of ZnS primarily affects NIR property while leaving MIR performance unaffected. To delve deeper into the physical mechanism, we examine the electric fields at 1.064 μm and 1.55 μm for both IST states. Figure 3(d) and 3(e) illustrate the electric field distributions at 1.064 μm and 1.55 μm in the aIST state, respectively. From the electric field intensity distribution, we observe that the electric field strength is primarily concentrated in the ZnS and the top Ge layer. The medium-metal surface created by the ZnS/Ge interface can excite plasma resonance. Meanwhile, since the substrate is metallic, the lower layer material forms a Fabry-Pérot (F-P) cavity, causing the light to undergo multiple reflections and thereby enhancing absorptivity. Similar field localization phenomena are observed in the cIST state, as shown in Fig. 3(g) and Fig. 3(h) for 1.064 μm and 1.55 μm, respectively. Unlike the amorphous state, the IST in the crystalline state exhibits akin to metallic behavior. Therefore, in the electric field distributions at 1.064 μm and 1.55 μm, the lower layer (Cr and IST) acts as a metallic mirror, while the light undergoes multiple reflections within the Ge/TiO_2/Ge structure, thereby enhancing absorptivity. Figure 3(f) shows the 10.6 μm electric field in the aIST state, and we observe that the electric field intensity is mainly concentrated in the TiO_2/Ge/IST layer. This behavior can be attributed to the unique optical property of Ge, which exhibits a high extinction coefficient in the visible band but becomes relatively transparent in the infrared band, enabling energy penetration into the substructure. When the IST is in the amorphous state, so the lower Ge and the upper and lower two dielectric layers form F-P cavity that localizes the energy to the lower Ge[52–54]. Meanwhile, we observe strong electric field distribution around the ZnS. However, the reflectivity spectra in Fig. 3(b) reveal that the presence or absence of ZnS has no significant impact on the absorptivity at 10.6 μm. This is because ZnS and Ge form propagating plasmonic resonance on the surface in the MIR and LWIR, which do not affect the device's infrared performance. In these spectral bands, the infrared response is primarily governed by the internal resonant modes of the device. Further analysis of the thermal management window mechanism is conducted through electric field examination at the characteristic wavelength of 7.4 μm. Figure 3(i) shows the 7.4 μm electric field distribution in the cIST state, and we observe that the electric field intensity is mainly concentrated in the Ge/TiO_2/Ge layer. The electric field energy is localized in the TiO_2 layer, because the IST is close to metal when it is in the cIST state. Next, the effective impedance of the device is calculated using S-parameters (scattering parameters). Analysis of the S-parameters reveals that the wavelengths corresponding to the minima in the imaginary parts of the S-parameters coincide with the resonance wavelengths[50,51] (see Supplementary information

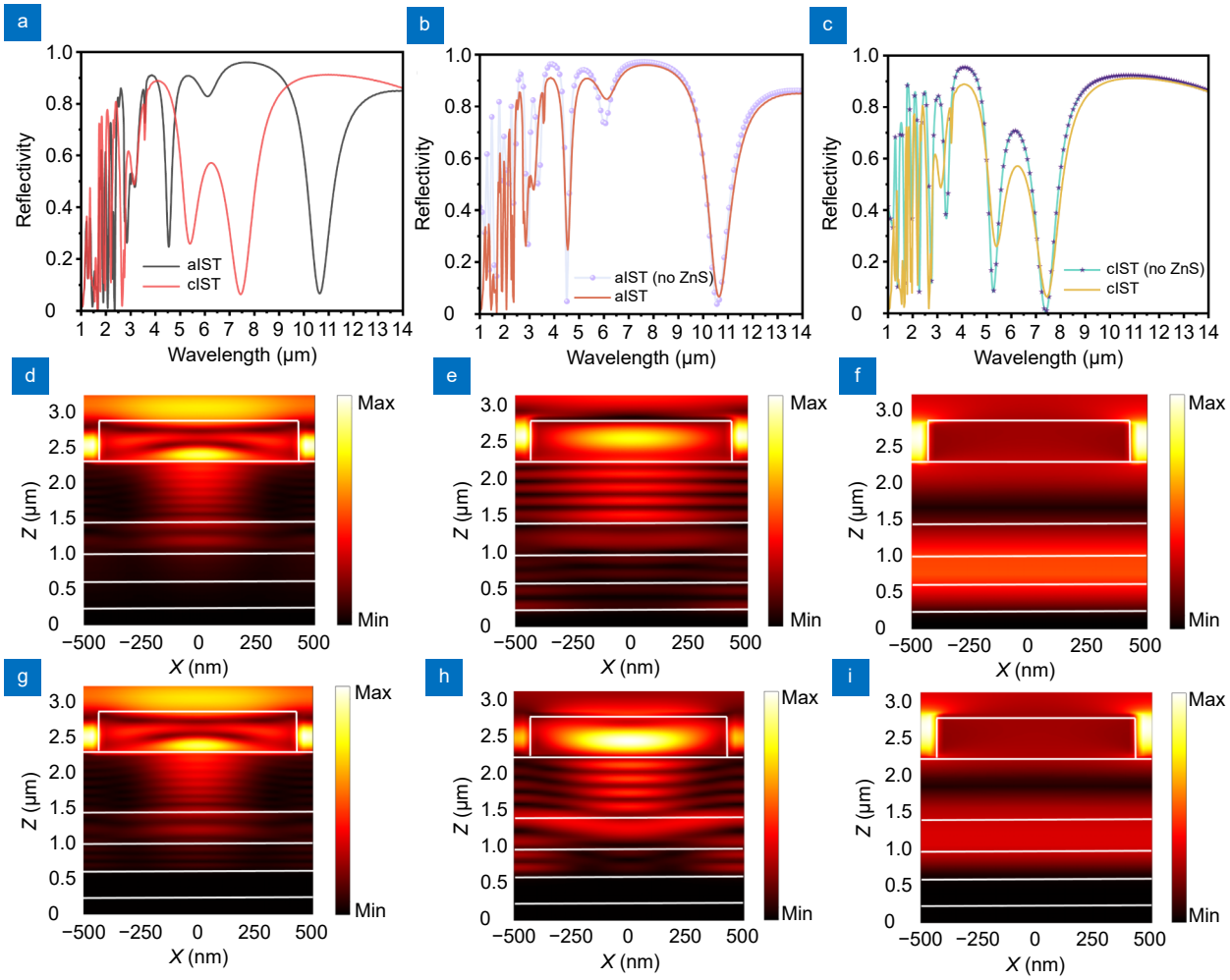

Fig. 3 | (**a**) Simulation infrared reflectivity spectra of the device in the aIST and cIST states. (**b**) Simulation infrared reflectivity spectra in the aIST and aIST (no ZnS) states. (**c**) Simulation infrared reflectivity spectra in the cIST and cIST (no ZnS) states. Electric field distributions in the aIST state: (**d**) 1.064 μm electric field distribution, (**e**) 1.55 μm electric field distribution, (**f**) 10.6 μm electric field distribution. Electric field distributions in the cIST state: (**g**) 1.064 μm electric field distribution, (**h**) 1.55 μm electric field distribution, (**i**) 7.4 μm electric field distribution.

of Fig. S2).

The current challenges in phase change material application primarily revolve around three critical aspects: phase change, reversibility, and patterning. The phase change characteristics are the basis for achieving different functional conversions through external excitation sources, while the reversible feature is key to realizing repeated conversions of different functions. Patterning is a process in which phase change materials achieve an intermediate state by altering their crystalline proportion, thereby adjusting their emissivity. To systematically investigate these properties in IST phase change material, we have developed a comprehensive laser experimental platform using a 532 nm laser as the excitation source, as illustrated in Fig. 4(a). Meanwhile, we conduct simulation on the spectral response of the thin film to the 532 nm laser, ensuring the 532 nm laser is suitable for phase change, reversibility, and patterning experiments (see Supplementary information of Fig. S3). Based on the laser experimental design diagram, we construct the specific laser experimental platform, as shown in Fig. 4(b). The optical path is divided into two segments, one is the laser phase change optical path and the other is the white light imaging optical path. In the laser phase change path, the laser beam undergoes sequential modulation through a series of optical components. The light path begins with laser emission, followed by reflection through a mirror, spatial filtering through a diaphragm, spectral purification via a filter, beam splitting, and finally focusing through an objective lens onto the sample surface mounted on a precision displacement stage. The white light imaging path, designed for real-time

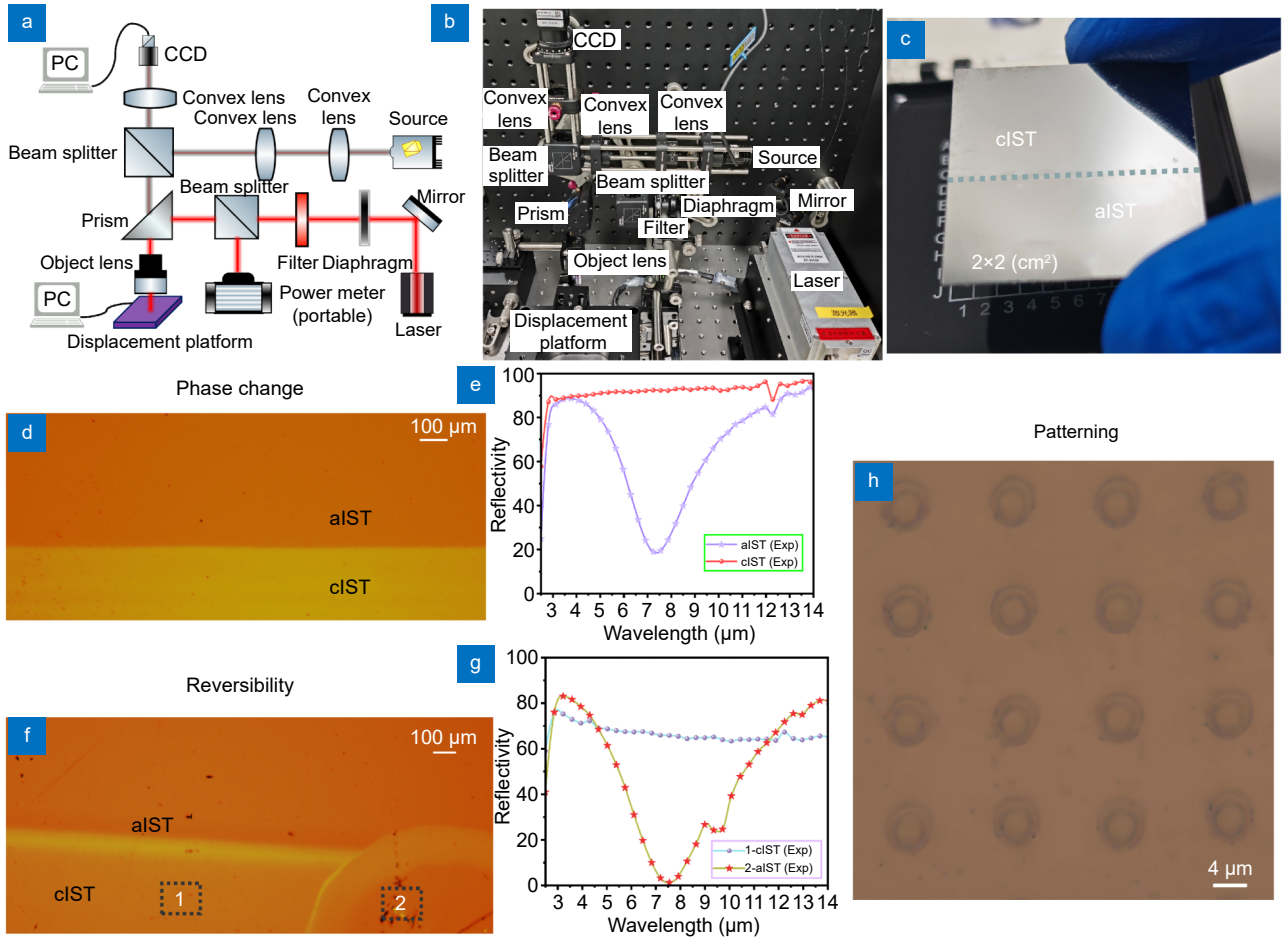

Fig. 4 | (**a**) Schematic diagram of the laser experimental platform. (**b**) Constructed laser experimental platform. (**c**) Schematic diagram of Cr/IST film phase change experiment (aIST to cIST). (**d**) Cr/IST/SiO_2 film phase change experimental (aIST to cIST) optical image. (**e**) Cr/IST film phase change experiment (aIST to cIST) infrared reflectivity spectra. (**f**) Cr/IST/SiO_2 film phase change (aIST to cIST)-reversibility (cIST to aIST) experiment optical image. (**g**) Cr/IST film phase change experiment (aIST to cIST) infrared reflectivity spectra. (**h**) Cr/IST thin film dot array image.

monitoring and characterization, initiates with white light emission. The light is collimated through a pair of convex lenses, directed through a beam splitter, and focused through an additional convex lens before being captured by a CCD detector. This configuration enables simultaneous imaging and data acquisition through computer interfacing, allowing for precise observation of phase change dynamics and pattern formation.

The experimental procedure begins with the preparation of a Cr/IST thin film through magnetron sputtering deposition, where the deposited IST naturally exists in the amorphous state. In the initial phase of our investigation, we perform laser-induced phase change experiment to achieve controlled crystallization of the IST. To initiate the phase change process, IST must be thermally elevated beyond its crystallization threshold around 292 °C[43]. The laser-induced phase change response exhibits pulse width dependence with a characteristic duration of approximately 10 ns[47]. The laser system operates at a frequency of 821 Hz with a driving current of 3600 mA, delivering an output optical power of 4.2 mW for precise phase change modulation. Following the laser irradiation process, a distinct visual contrast emerges between the irradiated and non-irradiated regions, as depicted in Fig. 4(c). The phase-changed region exhibits a characteristic metallic luster, while the untreated area maintains its original matte appearance. This visible transformation serves as the first indicator of successful phase change. To quantitatively verify the phase change completeness, we conduct infrared spectral analysis on both the amorphous (aIST) and crystalline (cIST) regions, as presented in Fig. 4(e). The spectral measurements reveal significant differences: the aIST region maintains its characteristic infrared absorptivity features,

while the cIST region demonstrates high reflectivity akin to metallic behavior. These spectroscopic results provide conclusive evidence of the successful and complete phase transformation from the amorphous to crystalline state, confirming the effectiveness of our laser-induced phase change methodology.

In the subsequent phase of our investigation, we focus on demonstrating the reversibility of the IST. To achieve reversibility, the material must be heated above its melting temperature (~626 °C) and then undergo rapid cooling, typically with cooling rates exceeding 10^9 K/s[43]. In the reversibility experiment, a higher laser energy is applied to melt the IST, followed by rapid cooling to achieve this transition. The reversibility of the laser-induced response demonstrates correlation with both the pulse bandwidth and cooling time, showing characteristic timescale of approximately 500 ns[47]. To prevent vaporization loss during IST melting, protective film is deposited on the IST surface. To facilitate this process, we first deposit an 80 nm SiO_2 protective layer on the Cr/IST thin film. This SiO_2 layer serves a critical function in preventing excessive IST vaporization during the high-temperature reversibility process, as evidenced in Fig. 4(d). In terms of phase change, similar results are achieved with the Cr/IST/SiO_2 film, as illustrated in Fig. 4(d). Subsequently, we implement the reversibility experiment in the "1" region (phase-change region), as depicted in Fig. 4(f). For this process, we employ a laser system integrated with an external pulse generator, configured with the following parameters: laser operating frequency of 820 Hz, operating current of 6000 mA, pulse generator frequency of 100 Hz, voltage levels of 5 V (high) and 0 V (low), and a duty cycle of 10%. Power meter measurement confirm an output optical power of 6.3 mW during the reversibility process. After the reversibility experiment is completed, it is observed that the color of the "2" region (reversibility region) closely resembles that of the non-phase-change region, as shown in Fig. 4(f). To quantitatively validate this reversibility, we perform infrared spectral analysis on both the phase-change ("1") and reversibility ("2") regions, as presented in Fig. 4(g). The spectral data demonstrate a complete transition cycle: "1" region shows the characteristic aIST to cIST transformation, while "2" region exhibits the reverse cIST to aIST transition. We also note the presence of a characteristic wavelength near 9.6 μm in the "2" region, which is generated by the SiO_2 intrinsic absorptivity peak. The combined evidence from optical microscopy and infrared spectroscopic analysis provides conclusive proof of successful phase change and reversibility in the IST material.

The final experiment focuses on demonstrating the patterning capability of the phase change material. Pixels are the basic units of patterns, so the fundamental challenge in achieving patterning lies in achieving pixelation. We successfully implement a laser-induced micro-patterning process on the Cr/aIST substrate, as demonstrated in Fig. 4(h). The experimental configuration employs the same laser parameters as those used in the phase change experiment, coupled with a pulse generator matching the reversibility experiment setting (100 Hz frequency, 5/0 V voltage levels, 10% duty cycle). Through precise control of single-pulse laser irradiation, we fabricate a 4×4 pixel array with remarkable precision on the Cr/aIST surface. Microscopic analysis reveals well-defined circular patterns with an average pixel diameter of 4 μm, demonstrating sub-wavelength scale patterning resolution. This successful implementation of high-density micro-patterning serves as concrete evidence of our laser platform's comprehensive capability in achieving three critical functions: controlled phase change, reversible switching, and precision microstructuring. The experimental results collectively validate the system's capacity to complete the full cycle of phase change material manipulation-from initial state modification through reversible transformation to final pattern realization.

After completing the phase change experiment, we use electron beam evaporation to prepare the thin film. Figure 5(a) illustrates the morphology of the multilayer film as characterized by Scanning Electron Microscopy (SEM). The SEM image clearly reveals the superior quality of the film. There is a noticeable boundary in the IST film layer, which is due to the first deposition being too thin and the second deposition being applied. During infrared spectroscopy measurement, we use the Ag film as the reference sample, since the reflectivity can reach 99%. Figure 5(b) and 5(c) present a comparison between the experiment and simulation results for the aIST and cIST states, respectively. We can observe that the aIST and cIST simulation and experiment results match well. The experiment results show that in the aIST state, the emissivities for the 3–5 μm and 8–14 μm are 0.38 and 0.29, respectively. The 10.6 μm wavelength absorptivity is 0.88. On the other hand, in the cIST state, the emissivities for the 3–5 μm and 8–14 μm are 0.36 and 0.08, respectively. The emissivities for the 5–8 μm and 2.5–3 μm are 0.55

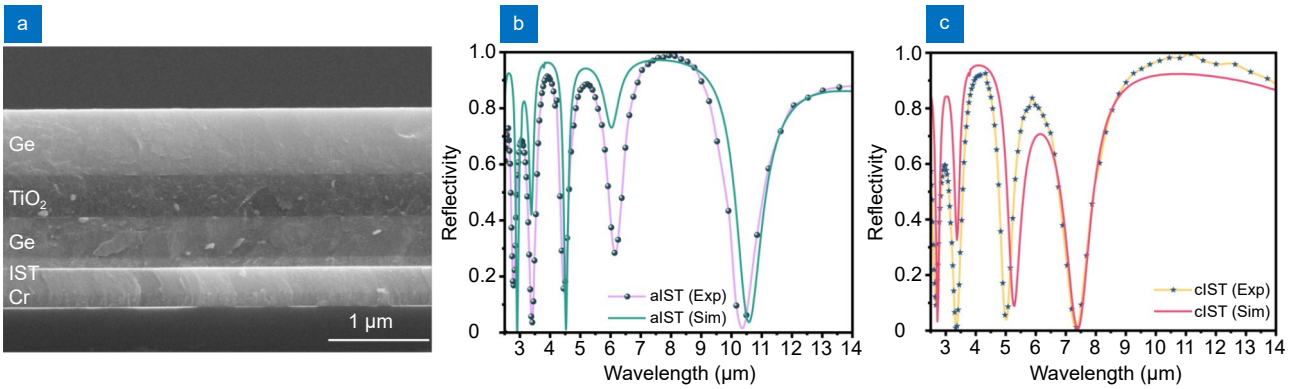

Fig. 5 | (**a**) SEM image of the sample. (**b**) Experiment and simulation infrared reflectivity spectra in the aIST state. (**c**) Experiment and simulation infrared reflectivity spectra in the cIST state.

and 0.62, respectively. These results clearly indicate the significant differences in thermal radiative properties between the amorphous and crystalline states of the IST material.

There are minor errors between the experiments and simulations, the main consideration is the error of the material parameters and thickness. From the perspective of material parameter error, the optical parameters of materials used in the simulation (such as refractive index, extinction coefficient) are obtained from the literature, but the thin films prepared in the experiment may deviate from the theoretical values due to purity and microscopic defects. From the thickness error, there is a 5%–10% manufacturing error between the thickness of the experimentally fabricated film and the theoretical design, which also causes the deviation between the experimental results and the simulation results.

Based on infrared spectroscopy data, there are significant differences between aIST and cIST. In the aIST state, the sample achieves simulated plant infrared camouflage in both 3–5 μm and 8–14 μm bands. In the cIST state, the sample attains simulated plant infrared camouflage in the 3–5 μm band and ultra-low emissivity infrared camouflage in the 8–14 μm band, while maintaining 2.5–3 μm and 5–8 μm bands as heat dissipation window bands. In the amorphous state, the sample achieves laser stealth at 10.6 μm. The laser stealth mechanism primarily involves absorbing energy at the laser wavelength, while simultaneously utilizing this energy as a source for the transition from aIST to cIST. We now proceed to further test the sample's infrared camouflage performance in the 3–5 μm and 8–14 μm bands.

To assess the effectiveness of infrared camouflage, we conduct tests in the 3–5 μm and 8–14 μm infrared spectra. As illustrated in Fig. 6(a), the leaves of the Rosaceae plant, Pyracantha fortuneana (Maxim.) Li, are chosen as the test samples, with fresh leaves used for each experiment. For comparison, Fig. 6(b) shows the selected control materials: Si wafer, C powder sheet, and Ag film. Figure 6(c) and 6(d) show the 3–5 μm infrared camouflage effect in the aIST and cIST states, respectively. As shown in Fig. 6(c), the top left corner and the top right corner represent C powder and Ag film, while the lower left corner and the lower right corner represent aIST sample and cIST sample, respectively. Figure 6(d) presents the same comparison from top to bottom: the C powder sheet, Ag film, aIST sample, and cIST sample. From these figures, it is evident that the C powder sheet exhibits high emissivity, while the Ag film exhibits low emissivity. As shown in Fig. 6(d), the emissivity is compared between the leaf and the four samples. We find that the emissivity of the aIST sample and the cIST sample is close to that of the leaf, so the colors they present are also similar. This indicates that the aIST and cIST samples achieve infrared camouflage effect similar to that of the leaf in the 3–5 μm spectrum.

Figure 6(e) and 6(f) illustrate the infrared camouflage performance in the 8–14 μm range for aIST and cIST states, respectively. As shown in Fig. 6(e), the top left corner and right corner depict the Si wafer and Ag film, respectively. The lower left corner and the lower right corner display the aIST and cIST samples, respectively. Similarly, Fig. 6(f) presents the Si wafer, Ag film, and cIST sample from top to bottom, with the aIST sample positioned between the leaf and the three samples. Data from Fig. 6(e) reveal that the surface emissivity temperatures of the Si wafer, Ag film, aIST sample, and cIST sample are 32.9 °C, 24.5 °C, 27.2 °C, and 24.8 °C,

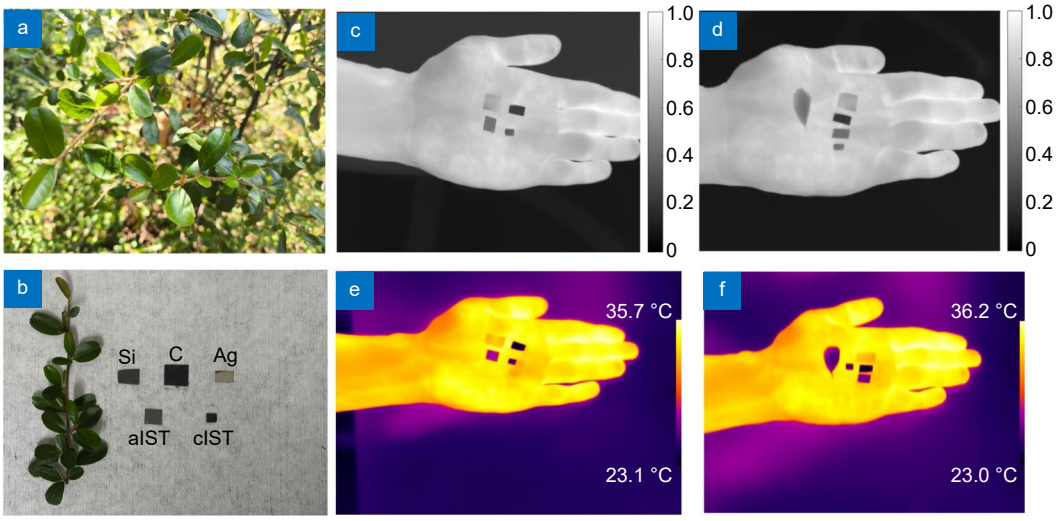

Fig. 6 | (**a**) Rosaceae-Pyracantha fortuneana (Maxim.) leaves. (**b**) Pyracantha fortuneana (Maxim.) leaves, Si wafer, C powder sheet, Ag film, aIST sample and cIST sample. 3–5 μm infrared camouflage performance: (**c**) C powder sheet (top left), Ag film (top right), aIST sample (bottom left) and cIST sample (bottom right); (**d**) C powder sheet, Ag film, aIST sample and cIST sample (from top to bottom). 8–14 μm infrared camouflage performance: (**e**) Si wafer (top left), Ag film (top right), aIST sample (bottom left) and cIST sample (bottom right); (**f**) Si wafer, Ag film, cIST sample (from top to bottom) and aIST sample (in the middle of the leaf and three samples).

respectively. The data from Fig. 6(f) show that the surface emissivity temperature of Si wafer, Ag film, aIST sample and cIST sample are 33.3 °C, 25.4 °C, 26.8 °C and 25.5 °C, respectively. The surface emissivity temperature of the leaf is 26.5 °C. Based on the infrared camouflage performance result within the 8–14 μm, it is observed that the temperature difference (ΔT) between the aIST surface and the leaf surface range from 0.3 °C to 0.7 °C, while the ΔT between the cIST surface and the Ag film is confined to 0.1 °C to 0.3 °C. The experiment are conducted in the ventilated environment. Due to the thermal management capability of the cIST sample, its temperature profile aligns more closely with that of the Ag film compared with the aIST sample. These results demonstrate dual camouflage functionality: the aIST state achieves effective infrared camouflage of biological specimens in the 8–14 μm band, whereas the cIST state enables infrared camouflage through emissivity suppression matching metallic coating. This bidirectional tunability suggests promising applications in adaptive camouflage systems requiring dynamic switching between natural environment blending and artificial surface concealment.

In order to verify the laser stealth function of the device, we use ion beam etching technology on the sample. First, based on the membrane system structure in Fig. 5, we continue to deposit ZnS thin film. It is important to note that ZnS material is not conductive. Consequently, prior to the ion beam etching experiment, it is imperative to apply a conductive adhesive on the sample surface via spin-coating. The selected conductive adhesive is an organic compound enriched with chromium ions and exhibits high solubility in water. As illustrated in Fig. 7(a), the sample is securely mounted using this conductive adhesive, ensuring effective electrical conductivity on both upper and lower surfaces through bilateral fixation. Post-experiment, residual conductive adhesive is thoroughly removed using distilled water. Figure 7(b) illustrates the top view of the SEM, whereas Fig. 7(c) depicts the side view of the SEM, inclined at an angle of 52° to the horizontal. We measure the cylindrical radius and thickness and find that the experiment is very close to the simulation. Next, we measure the NIR to LWIR reflectivity spectrum, as shown in Fig. 7(d). The infrared spectroscopy data demonstrates the absorptivity of 0.99 and 0.92 at 1.064 μm and 1.55 μm, respectively, in the aIST state, and the absorptivity of 0.96 and 0.74 at the same wavelengths in the cIST state. Meanwhile, we observe that the absorptivity at the 10.6 μm laser wavelength remains at 0.88 in the aIST state. It is noteworthy that the MIR infrared and LWIR infrared spectra closely resemble the infrared spectra depicted in Fig. 5, which also indicates that the top ZnS layer primarily influences the NIR band.

To characterize the laser stealth performance, the point cloud data obtained from 1.55 μm laser is used to

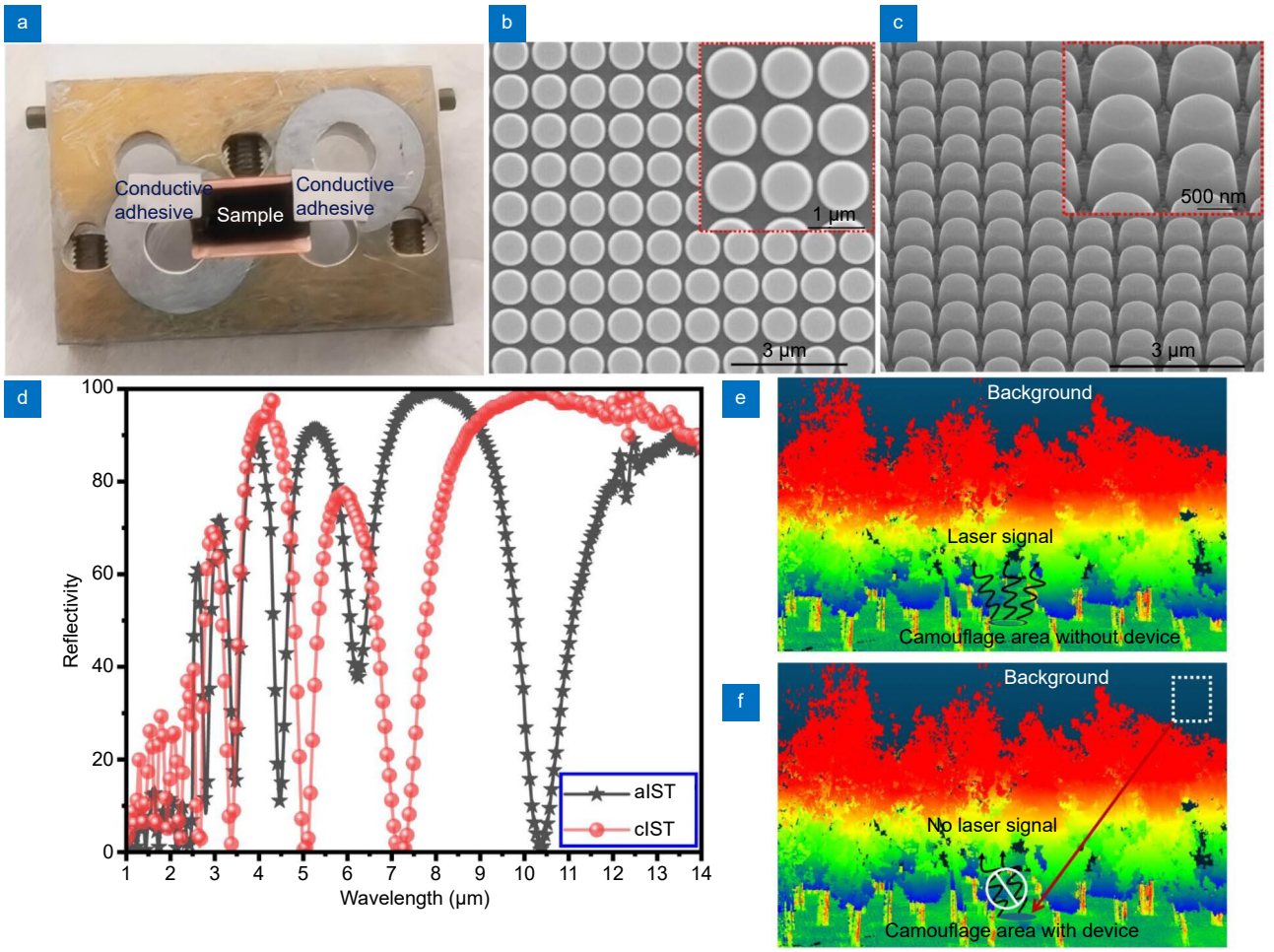

Fig. 7 | (**a**) Schematic diagram of the sample to be etched. (**b**) SEM top view of the device. (**c**) SEM 52° (angle with horizontal) side view of the device. (**d**) Infrared reflectivity spectra of the device in the aIST and cIST states. (**e**) The forest three-dimensional point cloud and the simulated laser stealth area. (**f**) Forest point cloud under laser stealth.

simulate laser stealth. As shown in Fig. 7(e), the laser three-dimensional point cloud data provides a forest image, where the elliptical region is simulated laser stealth region. Blue, yellow, and red represent the vertical distance of the object from the laser detector plane. Blue indicates closer proximity to the laser detector plane, while red indicates greater distance from the plane. As shown in Fig. 7(f), the elliptical area is covered with metamaterial structure, and the color presented is consistent with the background. The covering area absorbs the laser signal, resulting in no echo signal. Consequently, it will be classified as invalid point cloud data, thereby achieving laser stealth.

In the field of visible light camouflage, the primary goal is to either obtain high absorptivity or high transparency in the visible light band, or to match the color of the surrounding environment. In the visible spectrum, we not only achieve visible light camouflage through high absorptivity but also realize color changes by varying the structure parameters. The phase change material IST is a typical infrared material that behaves as a high-loss dielectric in the amorphous state and as a metal-like material in the crystalline state. However, in the visible band, the difference between the optical parameters of its amorphous and crystalline states is negligible, resulting in insufficient color contrast[41]. Therefore, we modulate the top ZnS structure parameters to achieve the color changes. Initially, we alter the radius parameters of the ZnS cylinder, modifying the radii from 285 nm to 485 nm in 5 nm increments. Figure 8(a) depicts the visible spectra associated with these varying radii; numbers 1–5 represent radii of 285 nm to 485 nm, respectively. The absorptivity does not change significantly and remains around 0.8. The chromaticity coordinates of the numbers 1–5 are calculated based on the visible reflection spectra. These coordinates are as follows: (0.32, 0.33),

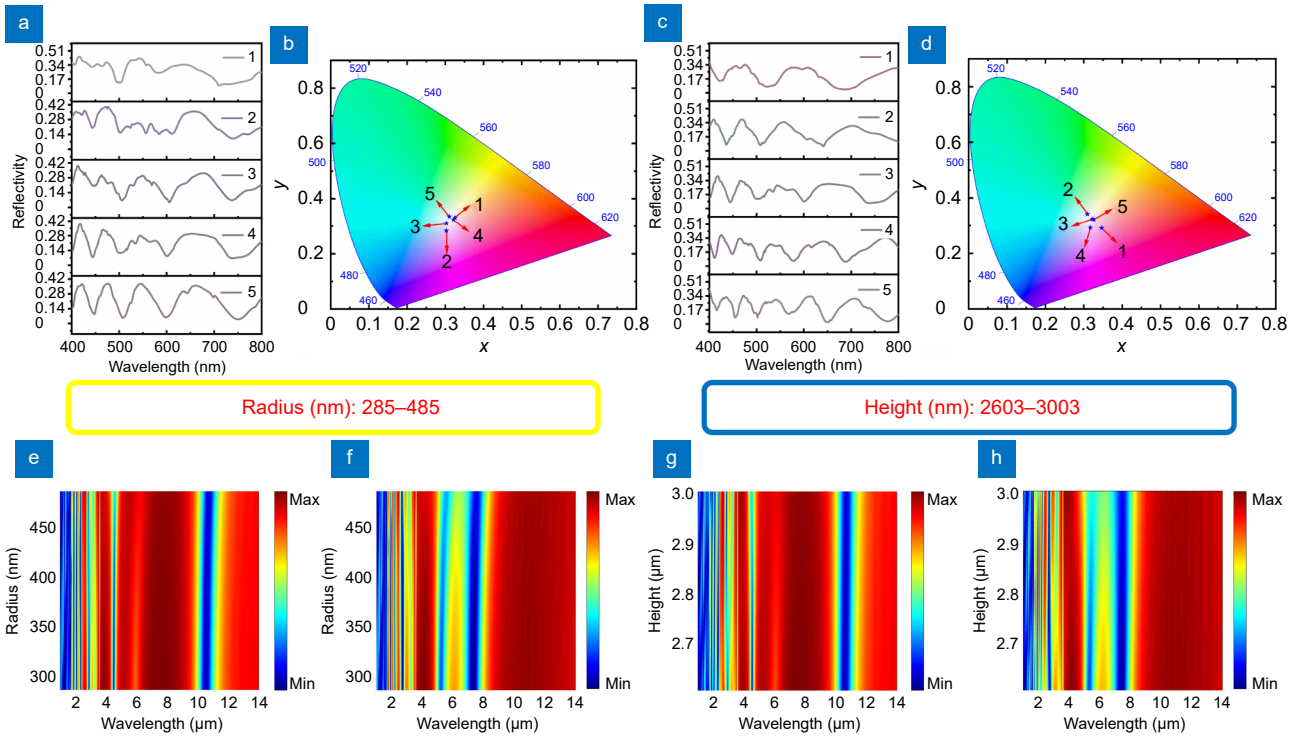

Fig. 8 | Color variations with changing radius parameter: (**a**) Visible reflectivity spectra for different radius parameters. (**b**) Chromaticity coordinates corresponding to different radius parameters. Color variations with changing thickness parameter: (**c**) Visible reflectivity spectra for different thickness parameters. (**d**) Chromaticity coordinates corresponding to different thickness parameters. aIST (**e**) and cIST (**f**) infrared reflectivity spectra for varying radius parameters. aIST (**g**) and cIST (**h**) infrared reflectivity spectra for varying thickness parameters.

(0.3, 0.28), (0.3, 0.31), (0.32, 0.32), and (0.31, 0.33), as shown in Fig. 8(b). If the radius parameters are changed, there is a significant effect on the infrared property, which is something we do not want to see. Therefore, we investigate the infrared spectra when changing the radius parameters. As illustrated in Fig. 8(e) and 8(f), we observe that changing the radius parameters do not affect the infrared property.

In a similar endeavor to achieve color change, we experiment with varying the thickness of the ZnS cylinder. We change the height parameters of the ZnS cylinder, varying the heights from 285 nm to 485 nm with the step size of 5. The absorptivity does not change significantly and also remains around 0.8, as shown in Fig. 8(c). The chromaticity coordinates of the numbers 1–5 are calculated based on the visible reflection spectra. These coordinates are as follows: (0.34, 0.29), (0.3, 0.34), (0.32, 0.33), (0.31, 0.29), and (0.32, 0.32), as shown in Fig. 8(d). Similarly, we investigate the infrared spectra when varying the thickness parameters. As illustrated in Fig. 8(g) and 8(h), we observe that varying the thickness parameters, there is no effect on the infrared property. To further analyze the applicability of the device, we perform analysis under different incident and polarization angles (see Supplementary information of Fig. S4). The device demonstrates superior performance under varying incident and polarization angles.

Table 2 shows a comparison of this work with the latest research results. We find that this work can be compatible with more functions and with the tunable performance. The research results show that in the visible light band, color camouflage can be achieved. In the infrared band, simulated plant camouflage and ultra-low emissivity camouflage can be realized. For laser stealth, high absorptivity at laser wavelengths of 1.06 μm, 1.55 μm and 10.6 μm can be achieved. Considering the structure heat dissipation requirement, the heat dissipation is managed at non-atmospheric window.

Conclusions

In summary, we successfully develop a comprehensive approach utilizing phase-change material IST to achieve a unified process integrating phase transition, reversibility, and patterning capabilities. Based on this, we design and fabricate a multispectral compatible infrared camouflage system based on IST. Our experimental results

Table 2 | Comparison of multispectral compatible infrared camouflage performance.

Reference (Simulation/Experiment)/ Structure	Switchable	Color camouflage	Thermal camouflage (ε 3–5 μm, ε 8–14 μm)		Infrared laser stealth (ε 1.064 μm, ε 1.55 μm, ε 10.6 μm)			Thermal management (ε 2.5–3 μm, ε 5–8 μm)	
ref.[11](Exp)	×	√	0.04	0.21	×	×	×	0.74	0.47
ref.[15](Exp)	√	×	0.03/0.8	0.46/0.25	×	×	×	×	×
ref.[36](Exp)	√	√	0.1	0.08	×	×	×	×	0.48
ref.[38](Exp)	×	√	0.25	0.33	×	×	0.9	×	0.7
ref.[55](Exp)	×	×	0.31	0.27	0.75	0.75	0.47	×	0.51
This work (Sim/aIST)	√	√	0.28	0.28	0.98	0.92	0.94	×	×
This work (Exp/aIST)	√	√	0.38	0.29	0.99	0.92	0.88	×	×
This work (Sim/cIST)	√	√	0.25	0.14	0.99	0.97	×	0.6	0.64
This work (Exp/cIST)	√	√	0.36	0.08	0.96	0.74	×	0.62	0.55

demonstrate successful phase transition from aIST to cIST using the laser platform, with verification through infrared spectroscopy. The reversible transition from cIST back to aIST is also accomplished using the same platform, confirmed by spectroscopic analysis. Furthermore, we achieve precise patterning through the fabrication of a 4 × 4 pixel dot array using the laser platform. Multispectral compatible infrared camouflage simulation shows that the presence of ZnS in the top layer only affects the NIR and has almost no effect on the MIR and LWIR. Further we use magnetron sputtering and electron beam evaporation processes to complete the film system structure (no ZnS) and measure the infrared camouflage effect. The experiment results show that the structure can realize infrared camouflage that simulates the plant (3–5 μm and 8–14 μm) in the aIST state. The structure can realize infrared camouflage that simulates the plant (3–5 μm) and ultra-low emissivity (8–14 μm) infrared camouflage in the cIST state. Next, we use the ion beam etching process to complete the fabrication of the top ZnS structure. The experiment results indicate that in the aIST state, the structure achieves high absorptivity at three laser wavelengths: 1.064 μm, 1.55 μm, and 10.6 μm. In the cIST state, the structure achieves high absorptivity at two laser wavelengths, 1.064 μm and 1.55 μm. Finally, we achieve the color change by changing the geometrical parameters of the top ZnS structure. The color change is achieved without affecting the infrared property of the structure. Consequently, our research successfully achieves the integration of phase change material IST with phase change, reversibility, and patterning processes. This opens up opportunity for reconfigurable imaging, reversible switching, and dynamic encoding of phase change material IST. Based on phase change material IST, the realization of tunable multispectral compatible infrared camouflage presents an effective countermeasure against multispectral detection technology.

References

1. Padilla WJ, Averitt RD. Imaging with metamaterials. *Nat Rev Phys* **4**, 85–100 (2022).
2. Liu TJ, Ou JY, MacDonald KF et al. Photonic metamaterial analogue of a continuous time crystal. *Nat Phys* **19**, 986–991 (2023).
3. Geng CC, Chen YY, Wei H et al. Adaptive variable emissivity reflector for seasonal and daily thermal regulation in regions with significant temperature variations. *Adv Funct Mater* **34**, 2410819 (2024).
4. Zaminga S, Martinez A, Huang HM et al. Optical chaotic signal recovery in turbulent environments using a programmable optical processor. *Light Sci Appl* **14**, 131 (2025).
5. Koepfli SM, Baumann M, Koyaz Y et al. Metamaterial graphene photodetector with bandwidth exceeding 500 gigahertz. *Science* **380**, 1169–1174 (2023).
6. Fu SQ, Zhang W, Wu Y et al. Bioinspired porous anodic alumina/aluminum flake powder for multiband compatible low detectability. *ACS Appl Mater Interfaces* **14**, 8464–8472 (2022).
7. Zhu HZ, Li Q, Tao CN et al. Multispectral camouflage for infrared, visible, lasers and microwave with radiative cooling. *Nat Commun* **12**, 1805 (2021).
8. Feng XD, Pu MB, Zhang F et al. Large-area low-cost multiscale-hierarchical metasurfaces for multispectral compatible camouflage of dual-band lasers, infrared and microwave. *Adv Funct Mater* **32**, 2205547 (2022).
9. Lin ZH, Wu QL, Liu XQ et al. Flexible meta-tape with wide gamut, low lightness and low infrared emissivity for visible-infrared camouflage. *Adv Mater* **36**, 2410336 (2024).

10. Kim J, Park C, Hahn JW. Metal-semiconductor-metal metasurface for multiband infrared stealth technology using camouflage color pattern in visible range. *Adv Opt Mater* **10**, 2101930 (2022).
11. Qin B, Zhu YN, Zhou YW et al. Whole-infrared-band camouflage with dual-band radiative heat dissipation. *Light Sci Appl* **12**, 246 (2023).
12. Shim HB, Han K, Song J et al. A multispectral single-layer frequency selective surface absorber for infrared and millimeter wave selective Bi-stealth. *Adv Opt Mater* **10**, 2102107 (2022).
13. Xu ZQ, Luo H, Zhu HZ et al. Nonvolatile optically reconfigurable radiative metasurface with visible tunability for anticounterfeiting. *Nano Lett* **21**, 5269–5276 (2021).
14. Cui G, Peng Z, Chen XY et al. Freestanding graphene fabric film for flexible infrared camouflage. *Adv Sci* **9**, 2105004 (2022).
15. Jiang XP, Wang XF, Nong J et al. Bicolor regulation of an ultrathin absorber in the mid-wave infrared and long-wave infrared regimes. *ACS Photonics* **11**, 218–229 (2024).
16. Liu K, Lin ZY, Han B et al. Non-volatile dynamically switchable color display via chalcogenide stepwise cavity resonators. *Opto-Electron Adv* **7**, 230033 (2024).
17. Ma XL, Pu MB, Li X et al. All-metallic wide-angle metasurfaces for multifunctional polarization manipulation. *Opto-Electron Adv* **2**, 180023 (2019).
18. Woo HK, Zhou K, Kim SK et al. Visibly transparent and infrared reflective coatings for personal thermal management and thermal camouflage. *Adv Funct Mater* **32**, 2201432 (2022).
19. Li D, Chen QX, Huang JH et al. Scalable-manufactured metamaterials for simultaneous visible transmission, infrared reflection, and microwave absorption. *ACS Appl Mater Interfaces* **14**, 33933–33943 (2022).
20. Park C, Kim J, Hahn JW. Integrated infrared signature management with multispectral selective absorber via single-port grating resonance. *Adv Opt Mater* **9**, 2002225 (2021).
21. Huang JK, Wang YT, Yuan LM et al. Large-area and flexible plasmonic metasurface for laser-infrared compatible camouflage. *Laser Photonics Rev* **17**, 2200616 (2023).
22. Liu XH, Wang P, Xiao CY et al. Compatible stealth metasurface for laser and infrared with radiative thermal engineering enabled by machine learning. *Adv Funct Mater* **33**, 2212068 (2023).
23. Huang Y, Ma BZ, Pattanayak A et al. Infrared camouflage utilizing ultrathin flexible large-scale high-temperature-tolerant Lambertian surfaces. *Laser Photonics Rev* **15**, 2000391 (2021).
24. Yuan LM, Huang C, Liao JM et al. A dynamic thermal camouflage metadevice with microwave scattering reduction. *Adv Sci* **9**, 2201054 (2022).
25. Zhao M, Zhu HZ, Qin B et al. High-temperature stealth across multi-infrared and microwave bands with efficient radiative thermal management. *Nano-Micro Lett* **17**, 199 (2025).
26. Liu YC, Ma XM, Chao K et al. Simultaneously realizing thermal and electromagnetic cloaking by multi-physical null medium. *Opto-Electron Sci* **3**, 230027 (2024).
27. Nam J, Chang I, Lim JS et al. Flexible metasurface for microwave-infrared compatible camouflage via particle swarm optimization algorithm. *Small* **19**, 2302848 (2023).
28. Zhang ZC, Wang QY, Li ZF et al. A skin-beyond multifrequency camouflage system with self-adaptive discoloration and radar-infrared stealth. *Chem Eng J* **494**, 152867 (2024).
29. Wang YZ, Luo HL, Shao YZ et al. Detection and anti-detection with microwave-infrared compatible camouflage using asymmetric composite metasurface. *Adv Sci* **11**, 2410364 (2024).
30. Zhang JK, Zhao DP, Chen ZS et al. One dimensional photonic crystal based multilayer film with low IR and visible signatures. *Opt Mater* **91**, 261–267 (2019).
31. Liu B, Chen ZS, Li ZG et al. Design and preparation of multispectral stealth photonic crystals for visible light, infrared radiation, and 1.06 μm laser. *Opt Eng* **59**, 127107 (2020).
32. Deng ZC, Su YR, Qin W et al. Nanostructured Ge/ZnS films for multispectral camouflage with low visibility and low thermal emission. *ACS Appl Nano Mater* **5**, 5119–5127 (2022).
33. Kim T, Bae JY, Lee N et al. Hierarchical metamaterials for multispectral camouflage of infrared and microwaves. *Adv Funct Mater* **29**, 1807319 (2019).
34. Lee N, Lim JS, Chang I et al. Flexible assembled metamaterials for infrared and microwave camouflage. *Adv Opt Mater* **10**, 2200448 (2022).
35. Hosseini P, Wright CD, Bhaskaran H. An optoelectronic framework enabled by low-dimensional phase-change films. *Nature* **511**, 206–211 (2014).
36. Wang J, Wu ZX, Sun XY et al. Multi-band compatible camouflage enabled by phase transition modulation of flexible GST films. *Chem Eng J* **499**, 156128 (2024).
37. Du KK, Cai L, Luo H et al. Wavelength-tunable mid-infrared thermal emitters with a non-volatile phase changing material. *Nanoscale* **10**, 4415–4420 (2018).
38. Pan MY, Huang Y, Li Q et al. Multi-band middle-infrared-compatible camouflage with thermal management via simple photonic structures. *Nano Energy* **69**, 104449 (2020).
39. Zhou SH, Guo YM, Zhu LW et al. Continuous programmable mid-infrared thermal emitter and camouflage based on the phase-change material In_3SbTe_2. *Opt Lett* **48**, 4388–4391 (2023).
40. Liang SR, Xu F, Li WX et al. Tunable smart mid infrared thermal control emitter based on phase change material VO_2 thin film. *Appl Therm Eng* **232**, 121074 (2023).
41. Zhou SH, Dong SK, Guo YM et al. Colored thermal camouflage and anti-counterfeiting with programmable In_3SbTe_2 platform. *Nanophotonics* **13**, 945–954 (2024).
42. Zeng Y, Lu DZ, Xu XX et al. Laser-printed terahertz plasmonic phase-change metasurfaces. *Adv Opt Mater* **11**, 2202651 (2023).
43. Heßler A, Wahl S, Kristensen PT et al. Nanostructured In_3SbTe_2 antennas enable switching from sharp dielectric to broad plasmonic resonances. *Nanophotonics* **11**, 3871–3882 (2022).
44. Wei H, Gu JX, Zhao T et al. Tunable VO_2 cavity enables multispectral manipulation from visible to microwave frequencies. *Light Sci Appl* **13**, 54 (2024).
45. Liang SH, Guan H, Zhang HN et al. Intelligent Off/On switchable electromagnetic wave absorbing material based on VO_2 nanowires. *Chem Eng J* **489**, 151025 (2024).
46. Zhen JW, Song XX, Gan YJ et al. Classification of Rosaceae plants by infrared spectroscopy. *Laser Optoelectron Prog* **61**, 0930006 (2024).
47. Heßler A, Wahl S, Leuteritz T et al. In_3SbTe_2 as a programmable nanophotonics material platform for the infrared. *Nat Commun* **12**, 924 (2021).
48. Amotchkina T, Trubetskov M, Hahner D et al. Characterization of e-beam evaporated Ge, YbF_3, ZnS, and LaF_3 thin films for laser-oriented coatings. *Appl Opt* **59**, A40–A47 (2020).

49. Siefke T, Kroker S, Pfeiffer K et al. Materials pushing the application limits of wire grid polarizers further into the deep ultraviolet spectral range. *Adv Opt Mater* **4**, 1780–1786 (2016).
50. Demir A, Tabaru TE. O-ring shaped multiresonant wavelength selective plasmonic nanoemitter compatible with thermal management. *Plasmonics* **20**, 3429–3439 (2025).
51. Şanlı AK, Tabaru TE, Kılıç VT. Triple band diamond-shaped polarization insensitive plasmonic nano emitter for thermal camouflage and radiative cooling. *Opt Quant Electron* **56**, 1074 (2024).
52. Kats MA, Blanchard R, Genevet P et al. Nanometre optical coatings based on strong interference effects in highly absorbing media. *Nat Mater* **12**, 20–24 (2013).
53. Kats MA, Capasso F. Optical absorbers based on strong interference in ultra-thin films. *Laser Photonics Rev* **10**, 735–749 (2016).
54. Du KK, Li Q, Lyu YB et al. Control over emissivity of zero-static-power thermal emitters based on phase-changing material GST. *Light Sci Appl* **6**, e16194 (2017).
55. Feng XD, Zhang TQ, Liu XJ et al. Single-layer, cascaded and broadband-heat-dissipation metasurface for multi-wavelength lasers and infrared camouflage. *Opto-Electron Adv* **8**, 240280 (2025).

Acknowledgements

This research was funded by the National Key R&D Program of China (2022YFF0706005); National Natural Science Foundation of China (12272407, 62275269, 62275271，62305387); Foundation of NUDT (ZK23-03); Hunan Provincial Natural Science Foundation of China (2022JJ40552，2023JJ40683); State Key Laboratory of High Performance Computing, NUDT (202201-12); and the Hunan Provincial Innovation Foundation for Postgraduate, China (CX20230009).

Author contributions

X. Li designed the devices and wrote the original manuscript. X. Y. Liao, J. X. Zeng and X. Li performed the simulations and experimental characterization. X. Li, J. G. Wu fabricated the samples. J. B. Yang and Z. Yi proposed the original idea. X. He supervised the project. All authors reviewed and revised the manuscript with valuable suggestions.

Competing interests

The authors declare no competing financial interests.

Supplementary information

Supplementary information for this paper is available at https://doi.org/10.29026/oea.2025.250031